RSC Advances

PAPER

View Article Online
View Journal | View Issue

Cite this: *RSC Adv.*, 2025, **15**, 47399

Site-specific lithium adsorption and directional ion transport in Ti_2CO_2 MXenes: insights from nuclear magnetic resonance and climbing-image nudged elastic band calculations

Truc Anh Nguyen,[a] Nguyen Vo Anh Duy, †[bc] Duong Trong Nhan, [de] Tran Thi Nhu Bang,[a] Nguyen Truong Long, [b] Yoshiyuki Kawazoe [fgh] and Minh Triet Dang *[b]

Received 3rd October 2025
Accepted 25th November 2025

DOI: 10.1039/d5ra07509b

rsc.li/rsc-advances

The development of advanced anode materials is critical for improving the performance of lithium-ion batteries. Ti_2CO_2 MXene, with its metallic conductivity and rich surface chemistry, has emerged as a promising candidate; however, the fundamental processes of lithium adsorption and diffusion remain insufficiently understood. In this work, we employ first-principles calculations combined with nuclear magnetic resonance (NMR) analysis and climbing-image nudged elastic band (NEB) simulations to investigate the lithiation mechanism of Ti_2CO_2. NMR shielding tensors reveal the evolution of local electronic environments, from anisotropic Ti–O–Li interactions at low lithium coverage to delocalized charge redistribution at higher lithiation, thereby stabilizing adsorption sites. NEB simulations further identify anisotropic diffusion pathways, with a dominant low-barrier channel (0.09–0.24 eV) that remains active even under high loading. These results demonstrate that Ti_2CO_2 provides both structural resilience and electronic conductivity, highlighting its potential as an efficient host material for next-generation lithium-ion batteries.

1. Introduction

Since their commercialization by Sony in the early 1990s, rechargeable lithium-ion batteries (LIBs) have become indispensable in modern technology, powering applications ranging from smartphones and laptops to electric vehicles (EVs) and grid-scale energy storage systems.[1–3] The global shift toward clean transportation and renewable energy integration further underscores their pivotal role in reducing greenhouse gas emissions and enabling sustainable mobility. To meet the stringent requirements of EVs, energy storage systems must simultaneously deliver high reversible capacity, rapid charging, and long cycle life.[3–5] However, despite decades of progress, LIB technology continues to face critical challenges, including limited lithium resources, high production costs, and intrinsic electrode performance constraints.[6–8] Addressing these limitations is vital to meet the surging demand for mobile electronics and EVs while ensuring both economic and environmental sustainability. Consequently, the exploration of novel electrode materials and advanced electrochemical strategies has become a central theme in battery research, with efforts focused on improving storage capacity, ion transport, and electrical conductivity.[9,10]

MXenes, a family of two-dimensional transition metal carbides, nitrides, and carbonitrides, first reported in 2011,[11–17] have rapidly emerged as promising candidates for next-generation energy storage. With the general formula $M_{n+1}X_nT_x$ (where M is a transition metal, X is carbon or nitrogen, and T represents surface terminations such as O, OH, or F), MXenes exhibit metallic conductivity, large surface area, tunable surface chemistry, and mechanical stability. These unique attributes have made them attractive for applications in supercapacitors, lithium–sulfur,[16,18,19] sodium–sulfur,[15,20] and particularly lithium-ion[12,21,22] batteries. Unlike conventional electrodes such as $LiCoO_2$ and nickel-rich oxides,[23–26] which offer high energy density but suffer from cost, resource scarcity, and safety concerns,[27,28] Ti-based MXenes present a more sustainable alternative. Among these, $Ti_3C_2T_x$ has become the model system for lithium storage due to its robust Ti–C backbone and abundant surface functional groups.[29–32] The Ti–C framework provides mechanical integrity and metallic conductivity, while oxygen terminations act as strong Li^+ adsorption sites *via* Li–O

[a]*Can Tho University of Technology, 256 Nguyen Van Cu street, Can Tho City, Vietnam*
[b]*Can Tho University, 3-2 street, Can Tho City, Vietnam. E-mail: dmtriet@ctu.edu.vn*
[c]*FPT University, Can Tho Campus, 600 Nguyen Van Cu street, Can Tho City, Vietnam*
[d]*Laboratory for Computational Physics, Institute for Computational Science and Artificial Intelligence, Van Lang University, Ho Chi Minh City, Vietnam*
[e]*Faculty of Mechanical, Electrical, and Computer Engineering, Van Lang School of Technology, Van Lang University, Ho Chi Minh City, Vietnam*
[f]*New Industry Creation Hatchery Center (NICHe), Tohoku University, Sendai, Japan*
[g]*Department of Physics, SRM University-AP, Amaravati 522240, Andhra Pradesh, India*
[h]*School of Physics, Institute of Science and Center of Excellence in Advanced Functional Materials, Suranaree University of Technology, Nakhon Ratchasima 30000, Thailand*
† These authors contribute equally.

coordination.[33] These interactions enable reversible redox activity at Ti centers, giving rise to pseudocapacitive behavior and excellent rate performance. Moreover, the layered Ti–C–O structure accommodates lithium intercalation between sheets, where weak van der Waals interactions allow *c*-axis expansion without structural collapse. Enlarged interlayer spacing-achieved through oxygen termination, organic intercalation, or the formation of porous and scroll-like architectures-further enhances Li^+ accessibility and diffusion kinetics.[30]

Lithium storage in $Ti_3C_2T_x$ occurs through a dual mechanism: intercalation between Ti–C layers and adsorption at oxygen-rich sites. This combination of diffusion-controlled and capacitive processes enables high reversible capacity, ultrafast charge–discharge rates, and long cycle life. In addition, Ti–C-based composites can host secondary phases such as Si or Sn, with the MXene framework buffering their volume changes during cycling to improve stability. Collectively, these features position Ti-based MXenes as a new generation of electrode materials that unite high capacity, structural robustness, and strong surface interactions, paving the way for durable, high-performance LIBs.

Nevertheless, despite these advantages, a critical gap remains: the fundamental mechanisms of lithium adsorption and diffusion in MXenes, particularly Ti_2CO_2, are not yet fully understood. While it is recognized that surface terminations, interlayer spacing, and defects strongly influence ion transport, the details of how lithium prefers in-plane *versus* cross-plane diffusion pathways, how adsorption evolves with increasing coverage, and how these processes affect conductivity and structural stability remain unresolved. This lack of mechanistic insight limits the rational design and optimization of Ti_2CO_2 as an anode material.

In this study, we present a systematic first-principles investigation of lithium adsorption and diffusion on Ti_2CO_2 MXene to elucidate the underlying lithiation mechanism. The lithium-hosting capability of Ti_2CO_2 is examined through adsorption energy calculations across varying lithium concentrations, complemented by analyses of electronic structures, charge redistribution, and local bonding environments. Nuclear magnetic resonance (NMR) shielding tensors are employed to probe site-specific interactions and anisotropy, while climbing-image nudged elastic band (NEB) simulations are used to evaluate diffusion pathways and migration barriers. Our results reveal stable adsorption configurations, a semiconductor-to-metal transition upon lithiation, and highly anisotropic yet ultrafast Li-ion transport, with a dominant low-barrier diffusion channel persisting even under heavy loading. These findings highlight the potential of Ti_2CO_2 MXene as a structurally robust, electronically conductive, and high-performance anode material for next-generation lithium-ion batteries.

2. Computational details

All periodic density functional theory (DFT) optimizations were performed using the M3GNet-UP-2022 machine-learning (ML) potential, implemented in the Amsterdam Modeling Suite (AMS).[34,35] This potential set, trained using deep-learning algorithms, achieves an accuracy comparable to that of the generalized gradient approximation (GGA) with the Perdew–Burke–Ernzerhof (PBE) exchange–correlation functional.[36] Structural relaxations were performed until the stress energy per atom was below 10^{-5} Ha $Å^{-1}$, and the total energy change between successive steps was less than 10^{-6} Ha.

Electronic properties were further evaluated using the projector-augmented wave (PAW) method,[37] as implemented in the Vienna *ab initio* simulation package (VASP).[38,39] Brillouin-zone integrations employed an $7 \times 7 \times 1$ Monkhorst–Pack grid[40,41] with a plane-wave energy cutoff of 520 eV. The self-consistent field convergence threshold was set to 10^{-4} eV per cell, and geometry optimizations proceeded until the residual Hellmann–Feynman forces on each atom were smaller than 0.01 eV $Å^{-1}$. To eliminate interactions between periodic images, a vacuum spacing of 20 Å was applied along the out-of-plane direction. To ensure accuracy and reliability, Brillouin-zone integrations were employed using a Monkhorst–Pack scheme with a dense $11 \times 11 \times 1$ *k*-point grid to calculate the spatial charge densities.

To evaluate the stability of the adsorbed systems, the adsorption energy (E_{ads}) is the energy difference per atom between the total energy of the adsorbate–substrate system and the sum of the energies of the isolated adsorbate and pristine substrate, as follows[21,42]

$$E_{ads} = (E_{Li+MXenes} - E_{MXenes} - n_{Li}E_{Li})/n_{Li} \quad (1)$$

where $E_{Li+MXenes}$ and E_{MXenes} are the energies of the lithiated and pristine MXenes. E_{Li} is the energy per atom of a Li atom in its crystalline structure, and n_{Li} the number of Li atoms in the adsorbed systems. A more negative adsorption energy value indicates stronger binding and higher stability of the adsorption configuration.

Nuclear magnetic resonance (NMR) shielding tensors were obtained using the perturbative NMR extension of VASP, with a perturbation step size of 10^{-3} to ensure an accurate numerical evaluation of magnetic susceptibility derivatives. For these calculations, the plane-wave cutoff energy was increased to 600 eV, and the SCF threshold was tightened to 10^{-6} eV, providing a sufficiently large basis and stringent convergence for the reliable determination of NMR chemical shifts, similar to our recent calculations for the sodium lithium manganese oxide cathode materials.[43]

The charge–discharge performance is a key criterion in evaluating the suitability of a candidate material as an anode for lithium-ion batteries. To investigate lithium-ion diffusion, we employed the climbing-image nudged elastic band (NEB) method,[44,45] as implemented in the AMS package. The initial and final states of each diffusion pathway were obtained from fully optimized structures calculated using VASP, and nineteen intermediate images were used to describe each NEB trajectory. For comparison, analogous NEB calculations were also performed using the VASP implementation. To examine the influence of long-range dispersion interactions on the diffusion process, van der Waals (vdW) corrections were considered using three schemes: Grimme's DFT-D2 method,[46] the zero-damping

DFT-D3 method of Grimme,[47] and the Tkatchenko–Scheffler (DFT-TS) method.[48]

3. Results and discussion

3.1 Geometry optimization

In this study, we begin with the optimized pristine Ti_2CO_2 MXene substrate, which exhibits lattice constants of $a = b =$ 9.184 (Å), consistent with structural parameters thoroughly characterized in recent works.[15,17,19] The optimized structure of Ti_2CO_2 is shown in Fig. 1 (left panel). In the top view, the material exhibits a hexagonal lattice, in which Ti atoms (blue) form a layered framework that encloses the central C atoms (brown), while O atoms (red) symmetrically terminate the surface. The side view highlights the sandwich-like configuration, where oxygen layers on both sides cap the Ti–C–Ti backbone. This well-ordered architecture, combined with the stable oxygen termination, provides an abundance of active sites for adsorption and ensures structural robustness, making Ti_2CO_2 a promising substrate for subsequent studies on Li adsorption.

Building on the optimized structure of pristine Ti_2CO_2, we investigate the adsorption of lithium by systematically placing a single Li atom at various high-symmetry sites, including atop Ti atoms and other representative surface positions. The stability of each configuration is assessed through adsorption energy calculations using eqn (1), where more negative values indicate stronger binding and higher stability. The configuration with the lowest adsorption energy is identified as the most stable geometry and used as the reference state for further analyses. As shown in Table S1 of the SI, site #2 (Fig. S1a) exhibits the most negative adsorption energy among the nine possible adsorption sites, confirming it as the most energetically favorable binding site for a single Li atom on Ti_2CO_2. The inclusion of long-range van der Waals interactions, such as vdW-D2, vdW-D3, and vdW-TS, as presented in Table S2, even yields stronger adsorption energies. These results are consistent with recent findings reported in ref. 12.

To further evaluate the adsorption behavior, we extended the analysis to higher Li concentrations by sequentially introducing 2–9 Li atoms onto the Ti_2CO_2 surface, with nine atoms representing the maximum adsorption capacity of the chosen supercell. For each level of coverage, several initial configurations were tested to account for different adsorption geometries, and the most stable structures were identified based on their adsorption energies. This systematic stepwise approach provides a comprehensive picture of the lithiation process, from single-atom adsorption to saturated loading, and reveals how stability evolves with increasing Li content. The calculated adsorption energies are summarized in Table S1. Numbers in brackets correspond to the sites labeled in Fig. 1. Bold values indicate the most energetically favorable configuration for each lithium adsorption. For a single Li atom, the adsorption energy per atom is −38.18 m eV, dicating relatively weak binding but confirming that Ti_2CO_2 can accommodate Li adsorption, thereby establishing its potential as an anode material. Once the most favorable adsorption site was identified, additional Li atoms were sequentially introduced to simulate progressive lithiation (Fig. S1 and Table S1). Each configuration was fully relaxed to ensure structural stability, and the total adsorption energies were compared to determine the preferred lithiation pathways. In cases where multiple geometries yield identical adsorption energies, the Li atom closer to the center of the supercell was selected to reflect the behavior observed in the initial adsorption step. As the number of Li atoms increases, the adsorption energy becomes more negative, reaching ∼−192.99 m eV at full coverage with nine Li atoms. This monotonic decrease indicates that additional Li atoms experience stronger binding, likely due to cooperative effects and enhanced electrostatic interactions with the MXene surface. Importantly, no structural collapse was observed even at high concentrations, underscoring the robustness of the Ti–O and Ti–C framework. The steady stabilization with increasing Li content demonstrates that Ti_2CO_2 can accommodate multiple Li atoms without significant loss of binding strength, confirming its potential as

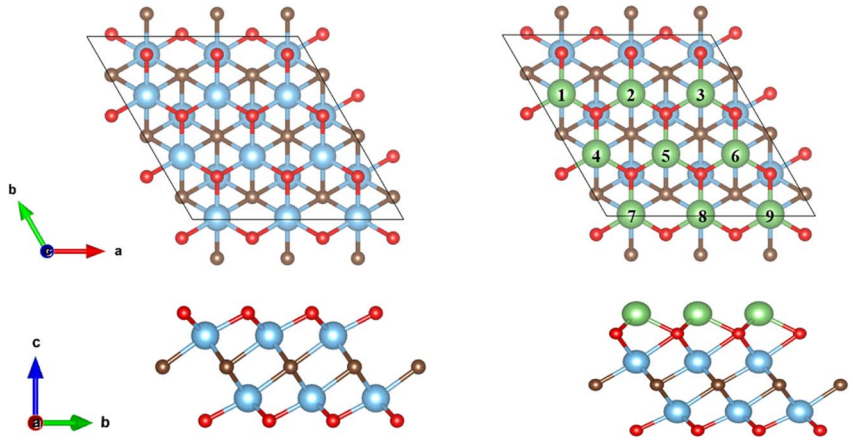

Fig. 1 Optimized crystal structures of pristine Ti_2CO_2 MXene (left) and Li-adsorbed Ti_2CO_2 (right). The top views show the hexagonal arrangement of Ti (blue), C (brown), and O (red) atoms, with Li atoms represented in green. Numbers 1–9 indicate the sequential adsorption sites for Li atoms on the MXene surface. The side views illustrate the layered configuration and the relative adsorption positions of Li atoms with respect to the Ti_2CO_2 substrate.

a stable and high-capacity anode material for lithium-ion batteries.

To further evaluate the dynamic stability of the pristine and Li-adsorbed Ti_2CO_2 MXene, we analyze the phonon dispersion spectra in Fig. 2. For the pristine Ti_2CO_2 (Fig. 2a), no imaginary frequencies are observed throughout the Brillouin zone, confirming the dynamic stability of the host lattice. The acoustic and optical branches are well separated, with the highest vibrational modes extending up to approximately 18 THz, reflecting the strong bonding interactions within the Ti–O and Ti–C framework. Upon adsorption of a single Li atom (Fig. 2b), the phonon spectrum remains free of imaginary modes, indicating that the incorporation of Li does not destabilize the lattice. The phonon branches display only minor modifications compared to the pristine structure, highlighting the robust structural tolerance of Ti_2CO_2 against initial lithiation. With a higher lithium content, such as five Li atoms (Fig. 2c), the vibrational spectrum becomes denser in the low-frequency region below 2 THz, which can be attributed to lattice distortions and local mass effects induced by Li adsorption. Nevertheless, the absence of negative frequencies demonstrates that the system maintains dynamic stability even at intermediate lithiation levels. At the highest coverage considered, with nine Li atoms adsorbed (Fig. 2d), low-frequency phonons are observed, which reflects enhanced electron–phonon interactions and stronger coupling between Li ions and the host lattice. However, this effect is not sufficient to trigger dynamic instability. Notably, the persistence of well-defined high-frequency optical modes demonstrates that the intrinsic Ti–O and Ti–C bonding remains intact under heavy lithiation. Overall, the phonon analysis confirms that Ti_2CO_2 maintains dynamic stability upon progressive lithiation, even at high Li concentrations. The absence of structural instabilities suggests that Ti_2CO_2 can effectively host Li ions without undergoing phase collapse, a prerequisite for long-term cycling stability. These results highlight the robustness of Ti_2CO_2 as a promising anode material for lithium-ion batteries, capable of accommodating multiple Li ions while preserving structural integrity.

3.2 Electronic properties

To elucidate electronic mechanisms in lithiated Ti_2CO_2 MXene, we combine orbital-resolved density of states and real-space charge density difference (CDD) with first-principles NMR calculations. The NMR shielding tensors (isotropic shifts and chemical shift anisotropy – CSA) serve as element-specific probes of bonding symmetry, electron delocalization, and

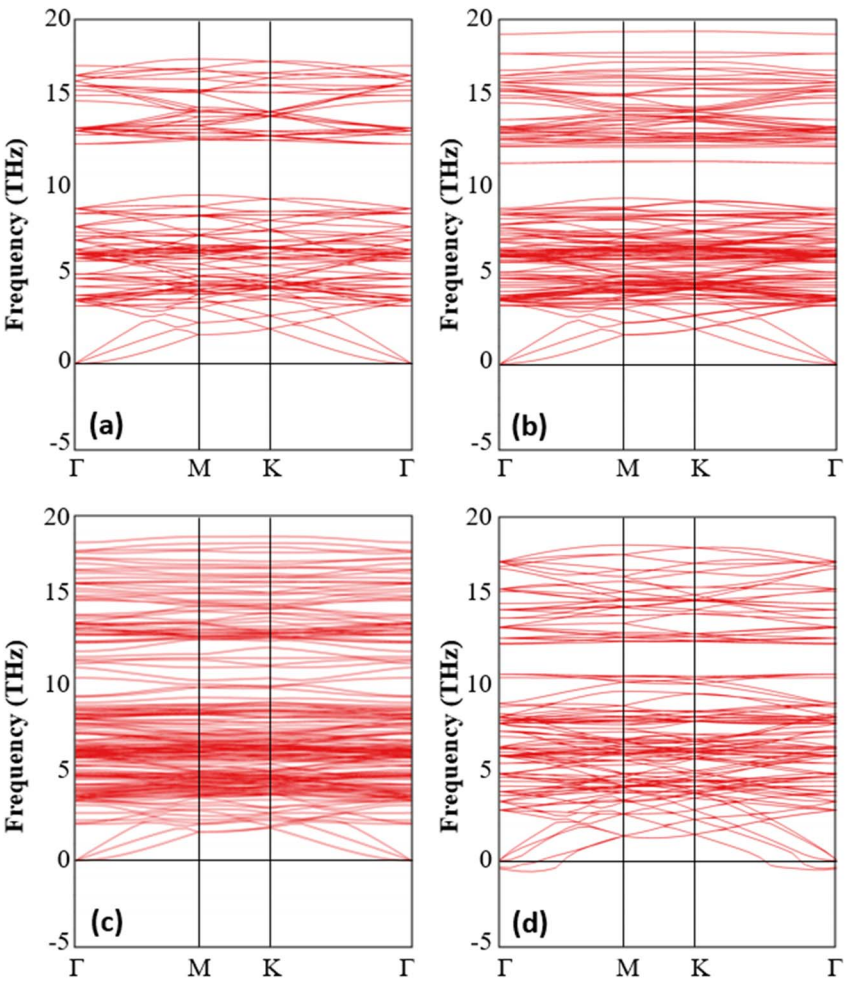

Fig. 2 Phonon dispersion spectra of pristine Ti_2CO_2 (a) and Ti_2CO_2 substrates adsorbed with 1 (b), 5 (c), and 9 (d) Li atoms.

local field gradients. Correlating these descriptors with Ti–O–Li hybridization and charge transfer explains how Li adsorption stabilizes distinct sublattices and enhances electronic conductivity.

Fig. 3 reveals a lithiation-driven semiconductor-to-metal transition in Ti_2CO_2. In the pristine state (Fig. 3a), the total density of states (TDOS) exhibits a small band gap, with the valence band dominated by O-2p and C-2p orbitals and the conduction band minimum arising from Ti-3d states, consistent with previous reports.[49,50] Upon initial Li adsorption (Fig. 3b), electron transfer from Li-2s orbitals introduces Ti-3d states at the Fermi level, closing the gap and initiating metallicity. As lithiation progresses, the density of states at E_F increases markedly, and at high coverage a pronounced peak develops, confirming robust metallic conductivity and enhanced carrier density. The charge density difference analysis in Fig. 4a and b further demonstrates localized charge accumulation around surface oxygen atoms and depletion near Li sites, underscoring the strong ionic interaction between Li and surface terminations and identifying oxygen as the primary electron acceptor. This localized stabilization at low coverage is crucial for initiating lithiation without compromising lattice integrity.

At intermediate coverage (five Li atoms), the PDOS reveals a marked increase in the density of Ti-3d and O-2p states at E_F, indicative of stronger Ti–O hybridization (Fig. 3c). In parallel, the CDD profiles (Fig. 4c and d) display more extensive charge accumulation along the O-terminated planes and broaden depletion zones around Li ions. These features highlight cooperative electrostatic interactions, where multiple Li ions reinforce one another's binding by promoting delocalized charge redistribution across the host lattice. The persistence of structural integrity in this state further confirms the robustness of the Ti–O and Ti–C backbone.

At saturated lithiation (nine Li atoms), the PDOS develops a pronounced Ti-3d-dominated peak at the Fermi level, confirming robust metallicity and high carrier density (Fig. 3d). The substantial orbital overlap between Ti-3d and O-2p states indicates that electron donation from Li is efficiently accommodated within the host lattice, thereby strengthening electronic transport pathways. The corresponding CDD maps (Fig. 4e and f) exhibit large, continuous regions of charge accumulation surrounding oxygen atoms and extended depletion near Li sites, demonstrating that charge redistribution becomes global rather than localized. This collective stabilization mitigates excessive electron localization, which is often associated with structural instabilities in heavily lithiated electrodes.

Overall, lithiation of Ti_2CO_2 proceeds through systematic charge transfer from Li-2s orbitals into the Ti–C–O framework, leading to progressive stabilization of oxygen redox centers, enhanced Ti–O hybridization, and a semiconductor-to-metal transition with high electronic conductivity. The strong agreement between PDOS and CDD analyses confirms that both

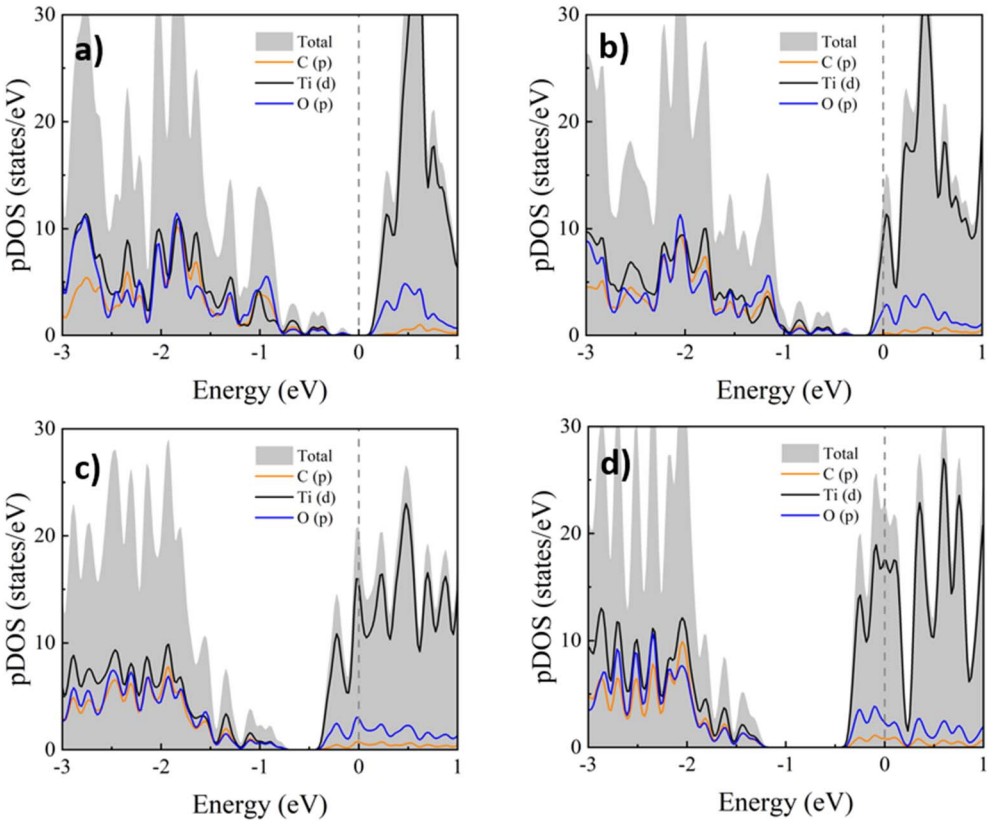

Fig. 3 Projected density of states (PDOS) of pristine Ti_2CO_2 (a) and Li-adsorbed Ti_2CO_2 with 1 (b), 5 (c), and 9 (d) Li atoms. The total DOS (shaded gray) is decomposed into contributions from C-p (orange), Ti-d (black), and O-p (blue) orbitals. The Fermi level set to zero is indicated by dashed lines.

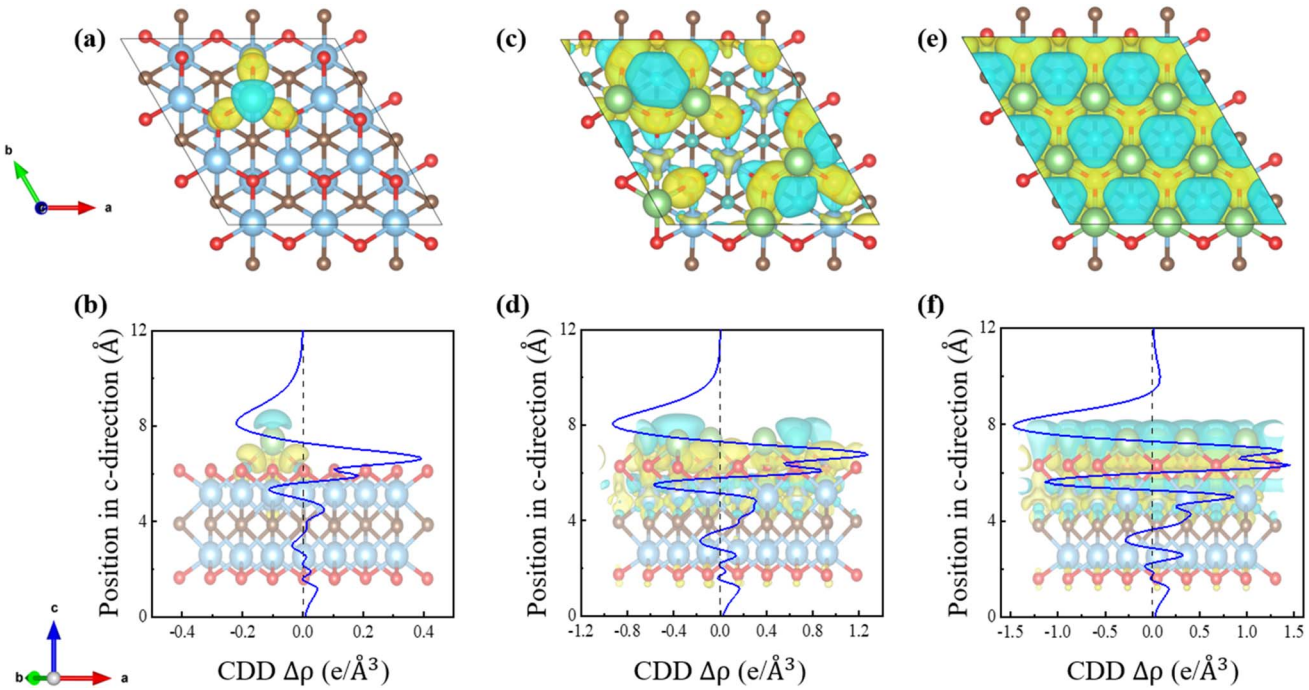

Fig. 4 The charge density difference (CDD) profiles along the *c*-direction upon adsorption of 1 (a and b), 5 (c and d), and 5 (e and f) lithium atoms. The iso-surface is set at 0.003 eÅ^{-3}. The yellow iso-surface indicates areas of charge accumulation, while the cyan iso-surface represents charge depletion.

localized and delocalized charge redistribution mechanisms underpin the superior electrochemical performance of Ti_2CO_2. This combination of structural robustness and improved electronic transport establishes Ti_2CO_2 as a promising candidate for lithium-ion battery anodes.

To further interrogate the role of nuclear-interaction anisotropy in lithium mobility, we extend our study to NMR spectra. In the pristine Ti_2CO_2 surface, both Ti and O nuclei exhibit strongly anisotropic shielding tensors, reflecting a rigid, directional Ti–O bonding network with localized charge density (Fig. S2 and Table S3). The introduction of a single lithium atom significantly alters this balance. Adsorption at the O_3 triangle above the Ti site results in a collapse of Ti anisotropy, reflecting a more symmetric local environment and partial averaging of the electric field gradients. This change corresponds to a situation where the Ti center becomes less restrictive, while oxygen atoms remain highly anisotropic due to the directional nature of Ti–O–Li bonding. The persistence of large oxygen chemical shift anisotropy values suggests that lithium is bound in a localized and directional site, limiting its immediate mobility but stabilizing the first stage of adsorption. This contrast signifies that the first Li atoms occupy O-coordinated hollows, which symmetrize the electric-field gradients around Ti while preserving directional Ti–O–Li interactions about the oxygen. The resulting local environments stabilize the initial adsorption state but maintain a relatively steep, site-specific potential around O, consistent with limited immediate mobility.

At intermediate coverage (five to six Li), Li–Li interactions and the attendant lattice response reintroduce anisotropy at Ti while progressively suppressing it at oxygen, and in a site-selective manner. The recovery of Ti CSA indicates an increasing structural distortion around metal centers, a predictable consequence of crowding and strain. In contrast, the marked reduction and unevenness of O CSA values reveal electrostatic screening of the O sublattice. This screening isotropizes the local fields experienced by oxygen along preferred directions, indicating the emergence of partially connected diffusion corridors between neighboring adsorption hollows. Concomitantly, the Li CSA remains modest, consistent with relatively symmetric local coordination and the onset of dynamic averaging.

At high coverage (eight to nine Li), Ti sites display strong anisotropy once again, whereas oxygen environments are comparatively isotropic. This inversion of the initial trend suggests that while the transition metal centers experience significant lattice distortions, the oxygen sublattice provides a smoother potential field. In practical terms, this configuration would facilitate lithium migration, since reduced anisotropy at O sites corresponds to a diminished energetic penalty for hopping between adjacent adsorption sites. Meanwhile, the modest CSA values observed for lithium itself across all loadings are consistent with relatively symmetric adsorption geometries and possible dynamic averaging, further supporting the notion that lithium is not firmly trapped once higher concentrations are reached.

A schematic picture of the lithium diffusion pathway can be inferred from the observed anisotropy trends. At low coverage, Li preferentially occupies stable sites above O_3 triangles, where strong Ti–O–Li interactions act as localized traps. With increasing lithiation, electrostatic repulsion and charge

redistribution reduce the anisotropy at oxygen sites, softening the energy landscape and opening low-barrier channels between adjacent adsorption sites. This evolution highlights that hollow sites between O-terminated triangles become the most favorable diffusion positions, providing energetically accessible pathways for Li hopping across the surface. At high coverage, screening of the oxygen lattice establishes quasi-continuous migration channels, while Ti distortions exert only a secondary influence on the potential profile. Thus, the progression of CSA values with lithiation reflects a transition from isolated binding pockets to interconnected hollow-site diffusion networks, which underpin both high storage capacity and rapid lithium transport in MXene-based electrodes.

3.3 Lithium-ion diffusion

The diffusion energy profiles and migration barriers of lithium ions are critical parameters for assessing the performance of lithium-ion battery anodes. A lower migration barrier indicates that lithium ions can move more easily along favorable diffusion pathways. Because the NEB method is computationally expensive, most studies in the literature report diffusion barriers for the transport of a single lithium ion. In this section, however, we investigate how varying lithium content affects the diffusion behavior of Li ions in Ti_2CO_2 MXenes, providing deeper insight into how diffusion properties evolve with increasing lithium concentration.

We first evaluate lithium-ion migration in Ti_2CO_2 MXene along two representative diffusion pathways (Fig. 5, 6, S3 and S4). Along path I, a single Li atom diffuses with a barrier of 0.386 eV. At moderate loading of five Li atoms, the barrier remains almost unchanged at 0.409 eV. Still, under heavy lithiation (nine Li atoms), the barrier dramatically increases to 2.210 eV, reflecting strong Li–Li interactions and lattice distortion that obstruct this pathway. Thus, path I is kinetically accessible only at low to moderate concentrations. In contrast, path II demonstrates consistently low diffusion barriers across lithiation states. For a single Li atom, the migration profile shows shallow side peaks of 0.027 eV and a maximum barrier of only 0.197 eV. At five Li atoms, the barrier remains modest at 0.243 eV, and under heavy lithiation with nine Li atoms, it decreases further to ~0.091 eV. This robustness highlights path II as the dominant conduction channel. Comparing the two pathways reveals pronounced anisotropy in lithium transport: path I, which corresponds to hopping between strongly bound O_3-top sites, becomes severely blocked at high coverage due to Li–Li repulsion and lattice distortions, consistent with CSA results showing localized charge trapping at these oxygen-coordinated sites. In contrast, path II follows hollow-site channels where CSA indicates softened anisotropy and delocalized charge redistribution, thereby preserving ultrafast ionic transport even under heavy lithiation and underscoring the directional nature of Li mobility in Ti_2CO_2.

Furthermore, Table 1 demonstrates that Li^+ mobility on Ti_2CO_2 is highly sensitive to both diffusion pathways and the

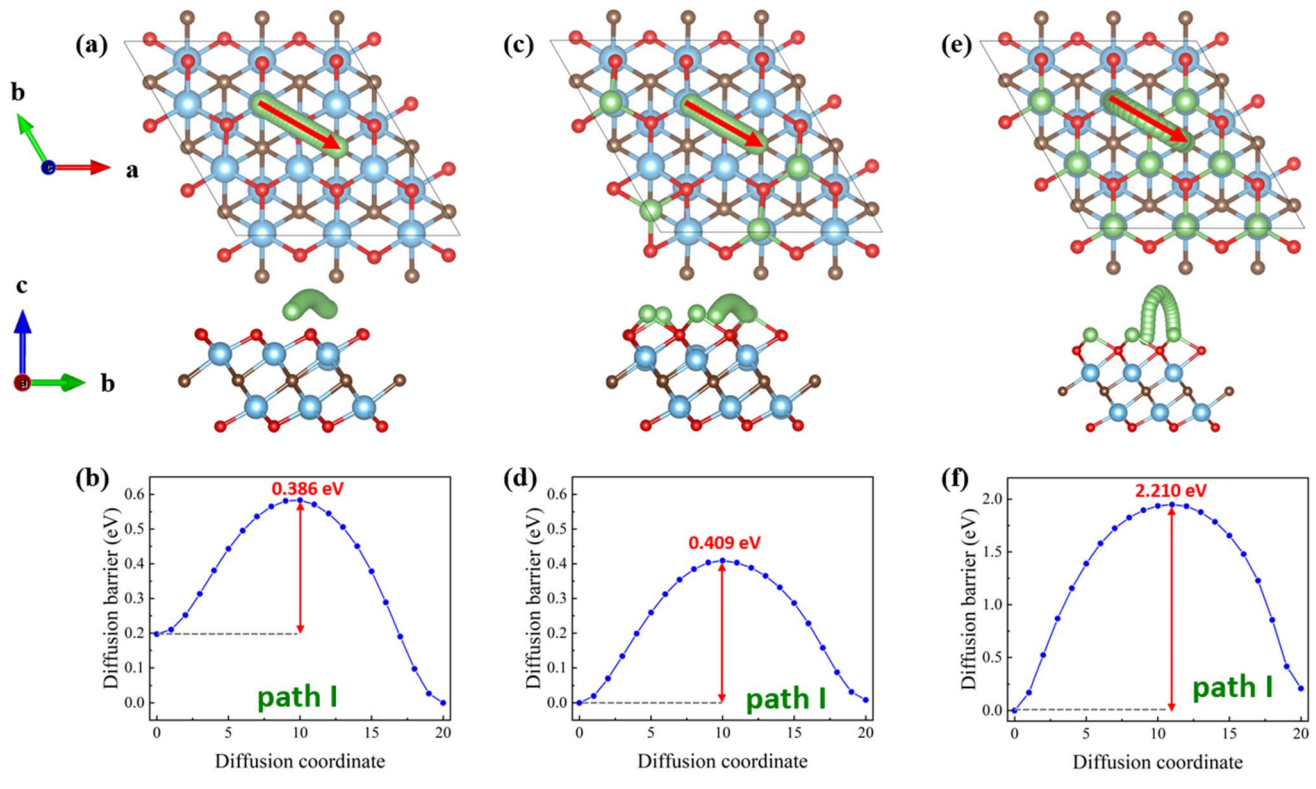

Fig. 5 The first lithium-ion diffusion pathway and corresponding energy barriers on Ti_2CO_2 MXene upon adsorption of 1 (a and b), 5 (c and d), and 9 (e and f) lithium atoms.

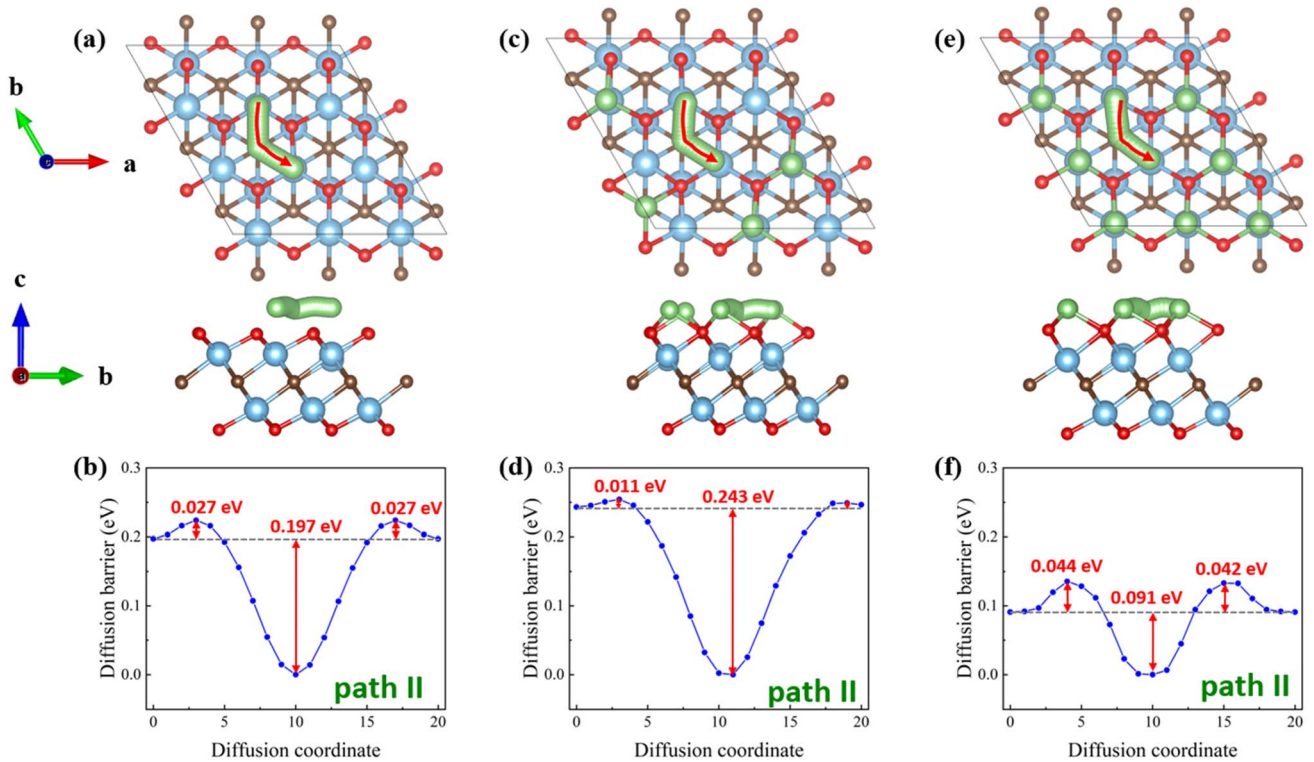

Fig. 6 The second lithium-ion diffusion pathway and corresponding energy barriers on Ti_2CO_2 MXene upon adsorption of 1 (a and b), 5 (c and d), and 9 (e and f) lithium atoms.

amount of intercalated lithium atoms. Along path I, the activation barrier is moderate at dilute and intermediate loadings, increasing only slightly from 0.386 eV (1 Li) to 0.409 eV (5 Li adsorption). The corresponding diffusivities are therefore limited, $D \sim 2.8 \times 10^{-8}$ and 1.1×10^{-8} cm^2 s^{-1}, which amount to merely 0.6% and 0.3% of the graphite benchmark (4.4×10^{-6} cm^2 s^{-1}). Upon heavy loading (9 Li), the situation changes drastically: the barrier surges to 2.21 eV and the diffusivity collapses by >30 orders of magnitude to 6.9×10^{-39} cm^2 s^{-1} (ratio ~0), indicating that path I becomes kinetically inaccessible at high coverage. In sharp contrast, path II preserves an ultralow barrier across the entire concentration range, 0.027 eV (1 Li), 0.011 eV (5 Li), and 0.044 eV (9 Li), and supports fast transport with $D \sim 3.0 \times 10^{-2}$, 5.4×10^{-2}, and 1.5×10^{-2} cm^2 s^{-1}, respectively. Normalized to graphite, these values are enhanced by roughly 6.7×10^3, 1.23×10^4, and 3.43×10^3 times, affirming a nearly barrierless diffusion channel that remains robust even under crowding. These results demonstrate that lithium diffusion along path II is intrinsically more favorable than along path I, due to the evolution of local environments during lithiation. In path I, Li moves between deep O_3-top adsorption wells that are strongly bound to Ti–O motifs. As concentration rises, Li–Li repulsion and Ti-centered distortions drastically increase the barrier, suppressing mobility. In contrast, path II follows a hollow-site corridor in which increasing lithiation screens the oxygen sublattice, flattens local field gradients, and maintains a smooth energy landscape. Consistent diffusion barriers and diffusion coefficients are also obtained when long-range van der Waals interactions are included, as shown in Fig. S5, S6 and Table S4. This screening effect lowers or maintains barriers even at high loading, keeping diffusion fast and robust, consistent with both the calculated energetics and the observed charge redistribution across the Ti–C–O framework.

Table 1 Diffusion barriers and corresponding diffusion coefficients of Li^+ ions on Ti_2CO_2 MXenes at different lithium coverages (1, 5, and 9 Li atoms) for two diffusion pathways (path I and path II)

Systems/characteristics	Path	Ti_2CO_2 + 1 Li	Ti_2CO_2 + 5 Li	Ti_2CO_2 + 9 Li
Diffusion barrier (eV)	I	0.386	0.409	2.21
	II	0.027	0.011	0.044
Diffusion coefficient (cm^2 s^{-1})	I	2.8×10^{-8}	1.1×10^{-8}	6.9×10^{-39}
	II	3.0×10^{-2}	5.4×10^{-2}	1.5×10^{-2}
The lithium diffusion coefficient ratio between Ti_2CO_2 and graphitic carbon[51] (4.4×10^{-6} cm^2 s^{-1})	I	0.006	0.003	0
	II	6719	12 280	3428

Compared to other electrode materials, the diffusion barriers of Ti_2CO_2 (0.09–0.41 eV along path II) are lower than those of graphite (0.3–0.6 eV), the standard for commercial LIB anodes.[16,51] They are also comparable to, or even superior to, other MXenes. For example, oxygen-terminated $Ti_3C_2O_2$ exhibits a barrier of 0.38 eV, while $Ti_3C_2S_2$ and $Ti_3C_2Se_2$ reduce the barrier to 0.23–0.16 eV.[12] Functionalized MXenes such as Cr_2Cse_2 and Mn_2CCl_2 reach barriers as low as ~0.02–0.05 eV.[16] The recently reported Ta_2Se_2C transition metal carbochalcogenides monolayer shows a Li-ion diffusion barrier of 0.26 eV,[52] while the best-performing nitrides (*e.g.*, Ti_2N, V_2N) exhibit barriers in the 0.01–0.03 eV range, values comparable to the lowest-barrier of Ti_2CO_2.[53] More exotic anodes, such as penta-graphene nanoribbons, have been reported with diffusion barriers of ~0.17–0.40 eV, which can be further reduced under applied electric fields.[42] Thus, these Ti_2CO_2 MXenes offer competitive transport, particularly through path II, positioning them as a strong candidate among MXenes and advanced 2D anodes. Beyond lithium-ion batteries, our recent investigations into these Ti_XCO_2 MXene hosts, where $X = 2$, 3, and 4, for sulfur cathodes in lithium–sulfur (Li–S) and sodium–sulfur (Na–S) batteries demonstrate complementary behavior.[15,17,19] In Li–S systems, heteroatom-doped MXenes (*e.g.*, N-doped Ti_3C_2) strengthen Li_2S adsorption and reduce diffusion barriers, thereby mitigating polysulfide shuttling. In Na–S systems, these Ti-based MXenes exhibit strong binding with Na_2S_x clusters (adsorption energies −1.8 to −3.2 eV), suppressing polysulfide dissolution and enhancing conductivity.[15] More recently, S- and N/S co-doped Ti_2CO_2 was shown to effectively anchor Na_2S_6 and Na_2S_8, with adsorption energies improved by up to 59% relative to pristine Ti_2CO_2, while simultaneously boosting electronic conductivity.[17,19]

Taken together, Ti_2CO_2 MXene exhibits anisotropic yet intrinsically fast Li-ion diffusion, competitive with and in some cases superior to graphite and conventional MXenes. When extended to Li–S and Na–S chemistries, surface modification strategies (doping and co-doping) further unlock its potential as a sulfur host by mitigating shuttle effects and enhancing conductivity. Thus, Ti_2CO_2 and its derivatives emerge as versatile platforms bridging both intercalation-type LIBs and conversion-type sulfur batteries, with diffusion anisotropy and surface chemistry engineering being key levers for performance optimization.

4. Conclusion

In this study, we employed DFT calculations to systematically investigate the adsorption energetics, electronic response, and transport properties of lithium ions on Ti_2CO_2 MXene. The results demonstrate that Ti_2CO_2 can accommodate multiple Li atoms without structural collapse, maintaining remarkable stability even at high lithiation levels. Progressive lithiation induces a semiconductor-to-metal transition, accompanied by a substantial increase in the pDOS near the Fermi level, ensuring robust electronic conductivity throughout the charge–discharge cycle.

A key novelty of this work is the combined use of first-principles NMR and NEB analyses, offering a uniquely detailed view of the lithiation mechanism. NMR analyses elucidate local bonding symmetry, charge redistribution, and directional interactions between Li ions and surface oxygen atoms, capturing the site-specific stabilization at low coverage and the emergence of delocalized charge redistribution at higher concentrations. Complementarily, NEB calculations resolve the directional anisotropy of Li-ion transport, identifying a dominant low-barrier pathway (0.09–0.41 eV) that remains accessible even under heavy lithiation. Such combinations offer a comprehensive mechanistic picture that could not be achieved through either approach alone.

These findings establish Ti_2CO_2 as a structurally robust and electronically conductive host with high adsorption capacity and intrinsically fast ion transport, outperforming conventional anodes such as graphite. Beyond Li-ion batteries, the proven ability of Ti-based MXenes to immobilize polysulfides and facilitate charge transfer highlights the broader versatility of this material platform, with promising implications for lithium–sulfur[16,18,19] and sodium–sulfur[15,20] chemistries. This dual-framework approach, combining NMR probes of local environments with NEB diffusion kinetics, provides a powerful strategy for rationally designing MXene-based electrodes and accelerating the discovery of multifunctional energy storage materials.

Conflicts of interest

There are no conflicts of interest to declare.

Data availability

The data supporting this article have been included as part of the supplementary information (SI). Supplementary information: adsorption energies of Ti_2CO_2 and Ti_2CO_2 + 1 Li calculated by various van der Waals exchange-correlation functionals; top and side views, NMR data and diffusion pathways and their corresponding activation energies of Ti_2CO_2 MXenes upon lithium adsorption at different Li concentrations. See DOI: https://doi.org/10.1039/d5ra07509b.

Acknowledgements

This research is funded by Can Tho University of Technology under Grant number DTCS 2024-12. Y. K. is supported by the Suranaree University of Technology (SUT), Thailand Science Research and Innovation (TSRI), and National Science, Research and Innovation Fund (NSRF) (NRIIS Project No. 90465). M. T. D. gratefully acknowledges the financial support provided by the Ministry of Education and Training, Vietnam (under Grant number B2024-TCT-16).

References

1 M. Li, J. Lu, Z. Chen and K. Amine, 30 Years of Lithium-Ion Batteries, *Adv. Mater.*, 2018, **30**(33), 1800561, DOI: 10.1002/adma.201800561.

2 M. Şen, M. Özcan and Y. R. Eker, A review on the lithium-ion battery problems used in electric vehicles, *Next Sustainability*, 2024, **3**, 100036, DOI: 10.1016/j.nxsust.2024.100036.
3 M. Ehsani, K. V. Singh, H. O. Bansal and R. T. Mehrjardi, State of the Art and Trends in Electric and Hybrid Electric Vehicles, *Proc. IEEE*, 2021, **109**(6), 967–984, DOI: 10.1109/JPROC.2021.3072788.
4 X. Zeng, M. Li, D. Abd El-Hady, *et al.*, Commercialization of Lithium Battery Technologies for Electric Vehicles, *Adv. Energy Mater.*, 2019, **9**(27), 1900161, DOI: 10.1002/aenm.201900161.
5 M. İnci, M. Büyük, M. H. Demir and G. İlbey, A review and research on fuel cell electric vehicles: Topologies, power electronic converters, energy management methods, technical challenges, marketing and future aspects, *Renew. Sustain. Energy Rev.*, 2021, **137**, 110648, DOI: 10.1016/j.rser.2020.110648.
6 J. Li, H. Liu, X. Shi, *et al.*, MXene-based anode materials for high performance sodium-ion batteries, *J. Colloid Interface Sci.*, 2024, **658**, 425–440, DOI: 10.1016/j.jcis.2023.12.065.
7 P. Komen, L. Ngamwongwan, S. Jungthawan, A. Junkaew and S. Suthirakun, Promoting Electrochemical Performance of $Ti_3C_2O_2$ MXene-Based Electrodes of Alkali-Ion Batteries *via* S Doping: Theoretical Insight, *ACS Appl. Mater. Interfaces*, 2021, **13**(48), 57306–57316, DOI: 10.1021/acsami.1c17802.
8 J. Li, D. Yan, S. Hou, *et al.*, Improved sodium-ion storage performance of $Ti_3C_2T_x$ MXenes by sulfur doping, *J. Mater. Chem. A*, 2018, **6**(3), 1234–1243, DOI: 10.1039/C7TA08261D.
9 R. Fang, S. Zhao, Z. Sun, D. W. Wang, H. M. Cheng and F. Li, More Reliable Lithium-Sulfur Batteries: Status, Solutions and Prospects, *Adv. Mater.*, 2017, **29**(48), 1606823, DOI: 10.1002/adma.201606823.
10 S. J. Tan, W. P. Wang, Y. F. Tian, S. Xin and Y. G. Guo, Advanced Electrolytes Enabling Safe and Stable Rechargeable Li-Metal Batteries: Progress and Prospects, *Adv. Funct. Mater.*, 2021, **31**(45), 2105253, DOI: 10.1002/adfm.202105253.
11 W. R. Sajal, Md M. Hassan, J. Islam, T. Sultan, Md B. Hossen and A. Arafat, Molecular dynamics study of mechanical stability of Ti_4C_3 MXene subjected to chirality, temperature, strain rate, and point-vacancy for Lithium-ion batteries, *Heliyon*, 2024, **10**(19), e38854, DOI: 10.1016/j.heliyon.2024.e38854.
12 M. Tian, Rational design of surface termination of $Ti_3C_2T_2$ MXenes for lithium-ion battery anodes, *Phys. Chem. Chem. Phys.*, 2025, **27**(9), 4717–4727, DOI: 10.1039/D4CP04583A.
13 T. Koriukina, A. Kotronia, J. Halim, *et al.*, On the Use of $Ti_3C_2T_x$ MXene as a Negative Electrode Material for Lithium-Ion Batteries, *ACS Omega*, 2022, **7**(45), 41696–41710, DOI: 10.1021/acsomega.2c05785.
14 M. Li, M. Xiao, B. Wang, Z. Li, H. Song and B. Xiao, Halogenated and chalcogenated Ti_2C MXenes: High capacity electrode materials for lithium-ion batteries, *Chem. Phys. Lett.*, 2023, **814**, 140356, DOI: 10.1016/j.cplett.2023.140356.
15 M. T. Dang, N. T. Long, V. B. Thi Phung, *et al.*, Resolving adsorption mechanism of sodium polysulfides on Tim+1CmO_2 MXenes for application in sodium-sulfur batteries: A first-principles study, *Appl. Surf. Sci.*, 2025, **687**, 162210, DOI: 10.1016/j.apsusc.2024.162210.
16 Z. Chen, Z. Chang, Z. Liu and N. Zhou, Functionalized M2CT2 (M = Ti, V, Cr, Mn; T = O, S, Se) MXenes as anchoring materials for lithium-sulfur batteries, *Appl. Surf. Sci.*, 2022, **602**, 154375, DOI: 10.1016/j.apsusc.2022.154375.
17 V. N. Nguyen, T. B. Trinh, T. L. Nguyen and M. T. Dang, First-principles insights into sulfur and nitrogen co-doped Ti_2CO_2 MXene as an advanced anchoring material for sodium polysulfides in sodium–sulfur batteries, *RSC Adv.*, 2025, **15**, 35586–35597.
18 T. Zhang, L. Zhang and Y. Hou, MXenes: Synthesis strategies and lithium-sulfur battery applications, *eScience*, 2022, **2**(2), 164–182, DOI: 10.1016/j.esci.2022.02.010.
19 T. L. Nguyen, B. T. Nguyen Thi, A. D. Nguyen Vo, T. H. Nguyen Thi and M. T. Dang, First-principles insights into selenium and sulfur doping on Ti_2CO_2 MXene for mitigating the shuttle effect in lithium-sulfur batteries, *Adv. Nat. Sci. Nanosci. Nanotechnol.*, 2025, **16**, 045008.
20 B. S. Reddy, G. B. Cho, N. S. Reddy, *et al.*, Layered-like structure of TiO_2-Ti_3C_2 Mxene as an efficient sulfur host for room-temperature sodium-sulfur batteries, *J. Alloys Compd.*, 2021, **883**, 160910, DOI: 10.1016/j.jallcom.2021.160910.
21 H. Kim, J. Choi, I. Bae, *et al.*, Functionalized MXene anodes for high-performance lithium-ion batteries, *J. Alloys Compd.*, 2025, **1010**, 177510, DOI: 10.1016/j.jallcom.2024.177510.
22 X. H. Li, S. S. Li, X. H. Cui, R. Z. Zhang and H. L. Cui, First-principle study of electronic properties and quantum capacitance of lithium adsorption on pristine and vacancy-defected O-functionalized Ti_2C MXene, *Appl. Surf. Sci.*, 2021, **563**, 150264, DOI: 10.1016/j.apsusc.2021.150264.
23 N. To Van, N. V. A. Duy, N. H. Hieu, *et al.*, Co-doping aluminum and boron enhances the stability and electrochemical properties of nickel-rich cathode materials for lithium-ion batteries, *Dalton Trans.*, 2025, **54**, 14173–14190, DOI: 10.1039/D5DT00528K.
24 T. Le Thi, T. Phan Van, B. Nguyen Van, *et al.*, Modified Coprecipitation Synthesis of Nickel-Rich NMC (Li1.0Ni0.6Mn0.2Co0.2O2) for Lithium-Ion Batteries: A Simple, Cost-Effective, Environmentally Friendly Method, *ACS Omega*, 2023, **8**(48), 45414–45427, DOI: 10.1021/acsomega.3c04717.
25 Y. Kim, Lithium nickel cobalt manganese oxide synthesized using alkali chloride flux: Morphology and performance as a cathode material for lithium ion batteries, *ACS Appl. Mater. Interfaces*, 2012, **4**(5), 2329–2333, DOI: 10.1021/AM300386J/SUPPL_FILE/AM300386J_SI_001.
26 G. Ko, S. Jeong, S. Park, *et al.*, Doping strategies for enhancing the performance of lithium nickel manganese cobalt oxide cathode materials in lithium-ion batteries, *Energy Storage Mater.*, 2023, **60**, 102840, DOI: 10.1016/j.ensm.2023.102840.

27 B. M. Gomes, M. C. Baptista, A. Orue, *et al.*, All-solid-state lithium batteries with NMC_{955} cathodes: PVDF-free formulation with SBR and capacity recovery insights, *Energy Mater.*, 2025, **5**(8), 500091, DOI: 10.20517/energymater.2024.297.

28 H. Banerjee, C. P. Grey and A. J. Morris, Stability and Redox Mechanisms of Ni-Rich NMC Cathodes: Insights from First-Principles Many-Body Calculations, *Chem. Mater.*, 2024, **36**(13), 6575–6587, DOI: 10.1021/acs.chemmater.4c00928.

29 R. Cheng, T. Hu, H. Zhang, *et al.*, Understanding the Lithium Storage Mechanism of Ti3C2Tx MXene, *J. Phys. Chem. C*, 2019, **123**(2), 1099–1109, DOI: 10.1021/acs.jpcc.8b10790.

30 Y. Jiang, Applications and perspectives of $Ti_3C_2T_x$ MXene in electrochemical energy storage systems, *Int. J. Electrochem. Sci.*, 2025, **20**(2), 100948, DOI: 10.1016/j.ijoes.2025.100948.

31 L. Liu, E. Raymundo-Piñero, S. Sunny, P. L. Taberna and P. Simon, Role of Surface Terminations for Charge Storage of $Ti_3C_2T_x$ MXene Electrodes in Aqueous Acidic Electrolyte, *Angew. Chem., Int. Ed.*, 2024, **63**(14), e202319238, DOI: 10.1002/anie.202319238.

32 P. Liu, P. Xiao, M. Lu, H. Wang, N. Jin and Z. Lin, Lithium storage properties of $Ti_3C_2T_x$ (Tx = F, Cl, Br) MXenes, *Chin. Chem. Lett.*, 2023, **34**(4), 107426, DOI: 10.1016/j.cclet.2022.04.024.

33 R. Santoy-Flores, H. N. Fernández-Escamilla, J. I. Páez-Ornelas, *et al.*, Nb2C and Nb2CO2 MXenes as Anodes in Li-Ion Batteries: A Comparative Study by First-Principles Calculations, *ACS Omega*, 2024, **9**(26), 28903–28911, DOI: 10.1021/acsomega.4c03603.

34 C. J. O. Verzijl and J. M. Thijssen, DFT-Based Molecular Transport Implementation in ADF/BAND, *J. Phys. Chem. C*, 2012, **116**(46), 24393–24412, DOI: 10.1021/jp3044225.

35 C. Chen and S. P. Ong, A universal graph deep learning interatomic potential for the periodic table, *Nat. Comput. Sci.*, 2022, **2**(11), 718–728, DOI: 10.1038/s43588-022-00349-3.

36 J. P. Perdew, Density-functional approximation for the correlation energy of the inhomogeneous electron gas, *Phys. Rev. B: Condens. Matter Mater. Phys.*, 1986, **33**(12), 8822–8824, DOI: 10.1103/PhysRevB.33.8822.

37 G. Kresse and D. Joubert, From ultrasoft pseudopotentials to the projector augmented-wave method, *Phys. Rev. B: Condens. Matter Mater. Phys.*, 1999, **59**(3), 1758, DOI: 10.1103/PhysRevB.59.1758.

38 G. Kresse and J. Hafner, *Ab initio* molecular-dynamics simulation of the liquid-metal–amorphous-semiconductor transition in germanium, *Phys. Rev. B: Condens. Matter Mater. Phys.*, 1994, **49**(20), 14251, DOI: 10.1103/PhysRevB.49.14251.

39 G. Kresse and J. Furthmüller, Efficiency of ab-initio total energy calculations for metals and semiconductors using a plane-wave basis set, *Comput. Mater. Sci.*, 1996, **6**(1), 15–50, DOI: 10.1016/0927-0256(96)00008-0.

40 H. J. Monkhorst and J. D. Pack, Special points for Brillouin-zone integrations, *Phys. Rev. B*, 1976, **13**(12), 5188, DOI: 10.1103/PhysRevB.13.5188.

41 T. N. Tran, M. T. Dang, Q. H. Tran, T. T. Luong and V. A. Dinh, Band valley modification under strain in monolayer WSe2, *AIP Adv.*, 2022, **12**(11), 115023, DOI: 10.1063/5.0127204.

42 T. N. Tran, N. V. Anh Duy, N. H. Hieu, *et al.*, Electric field enhances the electronic and diffusion properties of penta-graphene nanoribbon anodes in lithium-ion batteries, *RSC Adv.*, 2024, **14**(45), 33524–33535, DOI: 10.1039/D4RA05464D.

43 D. T. Nhan, N. V. A. Duy, N. C. Ben, *et al.*, Unraveling the electronic mechanisms of transition metal and fluorine co-doping for enhanced electrochemical performance in sodium lithium manganese oxide cathodes, *Dalton Trans.*, 2025, **54**, 16704–16717, DOI: 10.1039/D5DT00638D.

44 G. Henkelman, B. P. Uberuaga and H. Jónsson, A climbing image nudged elastic band method for finding saddle points and minimum energy paths, *J. Chem. Phys.*, 2000, **113**(22), 9901–9904, DOI: 10.1063/1.1329672.

45 G. Henkelman and H. Jónsson, Improved tangent estimate in the nudged elastic band method for finding minimum energy paths and saddle points, *J. Chem. Phys.*, 2000, **113**(22), 9978–9985, DOI: 10.1063/1.1323224.

46 S. Grimme, Semiempirical GGA-type density functional constructed with a long-range dispersion correction, *J. Comput. Chem.*, 2006, **27**(15), 1787–1799, DOI: 10.1002/jcc.20495.

47 S. Grimme, J. Antony, S. Ehrlich and H. Krieg, A consistent and accurate ab initio parametrization of density functional dispersion correction (DFT-D) for the 94 elements H-Pu, *J. Chem. Phys.*, 2010, **132**(15), 154104, DOI: 10.1063/1.3382344.

48 A. Tkatchenko and M. Scheffler, Accurate Molecular Van Der Waals Interactions from Ground-State Electron Density and Free-Atom Reference Data, *Phys. Rev. Lett.*, 2009, **102**(7), 73005, DOI: 10.1103/PhysRevLett.102.073005.

49 X. Gao, Y. Zhou, Y. Tan, *et al.*, Exploring adsorption behavior and oxidation mechanism of mercury on monolayer Ti_2CO_2 (MXenes) from first principles, *Appl. Surf. Sci.*, 2019, **464**, 53–60, DOI: 10.1016/j.apsusc.2018.09.071.

50 Y. Zhang, X. H. Zha, K. Luo, *et al.*, Tuning the Electrical Conductivity of Ti_2CO_2 MXene by Varying the Layer Thickness and Applying Strains, *J. Phys. Chem. C*, 2019, **123**(11), 6802–6811, DOI: 10.1021/acs.jpcc.8b10888.

51 K. Persson, V. A. Sethuraman, L. J. Hardwick, *et al.*, Lithium Diffusion in Graphitic Carbon, *J. Phys. Chem. Lett.*, 2010, **1**(8), 1176–1180, DOI: 10.1021/jz100188d.

52 N. F. Martins, J. A. S. Laranjeira, B. D. Aparicio-Huacarpuma, L. A. Ribeiro Junior and J. R. Sambrano, Computational Characterization of the Novel Ta2Se2C Transition Metal Carbo-Chalcogenide as Anode Material for Li and Na-Ion Batteries, *J. Phys. Chem. C*, 2025, **129**(37), 16559–16568, DOI: 10.1021/acs.jpcc.5c05097.

53 X. Zhao, P. Wang, E. Lv, *et al.*, Screening MXenes for novel anode material of lithium-ion batteries with high capacity and stability: A DFT calculation, *Appl. Surf. Sci.*, 2021, **569**, 151050, DOI: 10.1016/j.apsusc.2021.151050.